Alma Mater Studiorum Università di Bologna
Archivio istituzionale della ricerca

Dynamic Mapping of Electrochemiluminescence Reactivity in Space: Application to Bead-Based Assays

Dynamic mapping of electrochemiluminescence reactivity in space: application to bead-based assays

Dongni Han,[a,b] Danjun Fang,[b] Giovanni Valenti,[c] Francesco Paolucci,[c] Frédéric Kanoufi,[d] Dechen Jiang,*,[e] Neso Sojic*,[a]

[a] *Univ. Bordeaux, CNRS, Bordeaux INP, ISM, UMR 5255, ENSCBP, 33607, Pessac, France*

[b] *School of Pharmacy, Nanjing Medical University, Nanjing, Jiangsu, 211126, China.*

[c] *Department of Chemistry "G. Ciamician", University of Bologna, Via Selmi 2, 40126, Bologna, Italy*

[d] *Université Paris Cité, ITODYS, CNRS, F-75013 Paris, France*

[e] *State Key Laboratory of Analytical Chemistry for Life Science and School of Chemistry and Chemical Engineering, Nanjing University, Nanjing, Jiangsu, 210023, China*

Corresponding authors: dechenjiang@nju.edu.cn; sojic@u-bordeaux.fr

Abstract

As an electrochemical technique offering an optical readout, electrochemiluminescence (ECL) evolved recently into a powerful microscopy technique with the visualization of a wide range of microscopic entities. However, the dynamic imaging of transient ECL events did not receive intensive attention due to the limited number of electrogenerated photons. Here the reaction kinetics of the model ECL bioassay system was revealed by dynamic imaging of single $[Ru(bpy)_3]^{2+}$-functionalized beads in the presence of the efficient tripropylamine co-reactant. The time-profile behavior of ECL emission, the variations of the ECL layer thickness and the position of maximum ECL intensity over time were investigated, which were not achieved by static imaging in previous studies. Moreover, the dynamics of the ECL emission were confronted to the simulation. The reported dynamic ECL imaging allows investigating the ECL kinetics and mechanisms operating in bioassays and cell microscopy.

Introduction

After decades of fundamental research, electrochemiluminescence (ECL) is an analytical technique that has gained popularity in many fields, including imaging and bio-sensing.[1-6] The latter has led to successful commercial instruments for biomarker detection.[7-10] ECL is a luminescent phenomenon that is triggered by an electrochemical excitation and the signals are the current and the photons generated. Since it gives an optical readout, the spatial distribution of this signal can be mapped easily and offers the opportunity to perform microscopy experiments.[3, 4, 11-14] Given the high sensitivity and spatiotemporal controllability of ECL,[12, 15, 16] the combination between ECL and imaging enables the visualization of a variety of microscopic objects and cells.[8, 15, 17-26] ECL generation itself is a dynamic electrochemical process that integrates many elementary steps: the initial electrochemical reactions at the electrode surface, the exergonic electron-transfer reactions populating the excited state of the luminophore and finally its radiative relaxation to the ground state with the light emission. Most of the ECL imaging works study and visualize static entities such as micro/nano-particles, cells or organelles and require long exposure time of the 2D photodetector, (typically, a CCD camera).[27-36] Indeed, a few seconds or tens of seconds are classically used to accumulate enough photons in order to obtain a clear image of the analyzed objects.[4, 37-40] This is due to the low number of generated photons during the ECL process and to the limited ECL efficiency of the luminophores.[14] This limitation implies that dynamic processes in the subsecond or millisecond timescales are rarely investigated by ECL.[4, 41, 42] For example, Zhu and co-workers imaged the collisions of single $[Ru(bpy)_3]^{2+}$-doped silica nanoparticles by ECL with a 0.2 s exposure time.[41] Feng and co-workers reported the imaging of single ECL photons with an exposure time of 0.51 ms.[4] But, they needed 150 s to obtain an ECL image of a cell. Therefore, a clear need exists for the development of ECL microscopy with improved dynamics.

Thus, we report herein the dynamic ECL imaging of single $[Ru(bpy)_3]^{2+}$-functionalized microbeads. Such beads are widely used for ECL-based immunoassays and are successfully commercialized for the diagnostics. It is a very active area with different research facets, ranging from the synthesis of brighter ECL labels, to the deciphering of the mechanistic pathways, and to the development of original bio-assay strategies.[8, 9, 17, 21, 43-47] As a matter of fact, some of us previously reported a preliminary example of dynamic ECL imaging investigation of dye-doped silica nanoparticles anchored onto beads aimed at evaluating the

improving effect on the emission signal stability associated to the silica matrix in which the luminophores are embedded.[45]

The $[Ru(bpy)_3]^{2+}$ luminophore with the sacrificial tripropylamine (TPA) co-reactant forms a classical ECL system, which is the basis of a majority of immunoassays and DNA analysis.[48, 49] In commercial ECL assays, $[Ru(bpy)_3]^{2+}$-labeled analytes are immobilized on magnetic microbeads, which are attracted to the working electrode by a magnetic field. ECL emission is generated by imposing an anodic potential with the irreversible oxidation of TPA.[50] The "revisited route" proposed by Miao *et al.* involves the generation of the $[Ru(bpy)_3]^{2+}$ excited state, which is obtained by the electron-transfer reactions with the electrogenerated TPA radicals (i.e. without the direct oxidation of $[Ru(bpy)_3]^{2+}$ at the electrode surface).[51] This mechanistic pathway describes mainly the bead-based ECL emission. It is the predominant process for ECL emission within the diffusion distance of TPA radicals (about 3-4 μm).[52, 53] Mapping the ECL reactivity allowed to record the ECL behavior in 3D mode, to propose new reaction mechanisms, and simultaneously to study the complexity of the ECL mechanisms involving radicals with short-lifetimes.[8, 9, 17, 21, 49, 54, 55] As already mentioned, the research on ECL imaging mainly focuses on static imaging. However, with the uncovering of the complex kinetics in ECL reactions, static imaging has limited the description of those fast and tiny changes. Dynamic imaging of ECL processes has become a challenging task.

In this work, we performed dynamic imaging of the ECL reactivity in space to investigate the kinetics of $[Ru(bpy)_3]^{2+}$/TPA system at the single-bead level. The $[Ru(bpy)_3]^{2+}$ labels were attached to the microbead surface via sandwich immunoassay or amide covalent bond (Figure 1a). In this way, the immobilized $[Ru(bpy)_3]^{2+}$ centers are exposed to the electrogenerated TPA radicals. Top-view and side-view configurations (Figure 1b) enables to collect the optical signals in 3D mode with short exposure times (50 and 100 ms). Dynamic variations of ECL emission layer and instant ECL intensity on the single beads were recorded, providing kinetic information for the underlying electrochemical reactions. In comparison to the simulation, factors influencing the kinetic of ECL in the experimental conditions were found, which could support the optimization of ECL immunoassays.
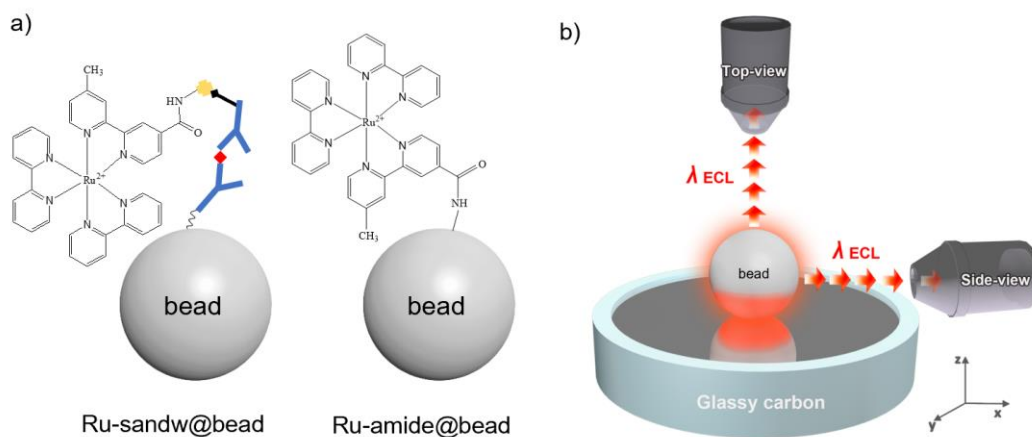
Figure 1. a) Polystyrene bead functionalized with the ECL label by sandwich immunoassay (left) or amide covalent bond (right). **b**) Scheme of the optical configurations used for dynamic ECL imaging of single labeled bead under the microscope: top-view and side-view.

Experimental section

Reagents. All the reagents were purchased from Sigma-Aldrich unless otherwise noted. polystyrene (PS) beads (diameter: 12 μm) were obtained from Kisker Biotech GmbH & Co. Capture antibody specific for interleukin 8 (IL-8), the complementary biotinylated detection antibody and IL-8 recombinant protein were obtained from R&D Systems Inc. TBS StartingBlock, PBS StartingBlock, and PBS Protein-Free blocking buffers were obtained from Pierce Biotechnology Inc. The streptavidin-modified $[Ru(bpy)_3]^{2+}$ complex used as an ECL label in the immunoassay experiments (i.e. Ru-sandw@bead) was synthesized according to the procedure reported previously.

Instrumentation. The electrochemical cell was a 3-electrode system: a working glassy carbon (GC) electrode, a platinum wire as the counter electrode and Ag/AgCl/KCl (3 M) electrode as the reference electrode. The experiments were performed using a μ-Autolab type III potentiostat. The PL and ECL images were recorded using an epifluorescence microscope from Leica (DMI6000, Leica Microsystems) and an Electron Multiplying Charge Coupled Device (EM-CCD 9100–13) Camera from Hamamatsu. PL and ECL experiments were performed in PBS containing 100 mM TPA (pH 7.4).

Immunoassay with PS beads (Ru-sandw@bead). The PS beads were labeled with the $[Ru(bpy)_3]^{2+}$ complex either by a sandwich immunoassay or by a peptidic bond. In the first case, antigen storage aliquots were prepared in PBS 1x/BSA 0.1% and detection antibody storage aliquots were prepared in tris-buffered saline (TBS StartingBlock). Each washing step was done in 100 μL of TBS with 1% Tween 20. The assay was performed by incubating for 2 h the microbeads functionalized with a capture antibody (anti-IL-8) first in a sample containing antigen (dilute to the appropriate concentration with PBS Starting Block) and washed. Then they were incubated for 30 min in 50 μL of the biotinylated detection antibodies solution (3 μg/mL of antibody in PBS StartingBlock) and washed. Finally, the ECL label was attached to form immunocomplex by exposing the beads to a solution containing a streptavidin-modified $[Ru(bpy)_3]^{2+}$ label.

Preparation of the Ru-amide@bead. The surface of the PS beads beared $-NH_2$ groups which allow further functionalization with the ECL $[Ru(bpy)_3]^{2+}$ label. 10 μL of beads suspension (2.5%) was washed with PBS (pH 7.4) and re-suspended in 1 mL of PBS. In the same time, 1 mg of $[Ru(bpy)_3]^{2+}$-NHS ester (bis(2,2′-bipyridine)-4′-methyl-4-carboxybipyridine-ruthenium N-succinimidyl ester-bis(hexafluorophosphate) was dissolved in 100 μL of dimethyl sulfoxide and this solution was added to the bead suspension. This mixture was incubated on +4 °C for 3 h with continuous stirring. After the incubation the beads were washed from reaction solution with PBS 10 times by the centrifugation for 10 min at 10,000 rpm to separate the beads from the solution. Finally, beads were suspended in 1 mL PBS and kept at 4 °C.

Results and discussion

We selected polystyrene (PS) beads with a diameter of 12 μm as the carrier of $[Ru(bpy)_3]^{2+}$ labels to record ECL images with good spatial resolution. The $[Ru(bpy)_3]^{2+}$ label decorates the bead using two functionalization procedures (Figure 1a). The first one is the sandwich immunoassay, in which the bead is modified with the capture antibody, the antigen, the biotinylated detection antibody and the streptavidin-modified $[Ru(bpy)_3]^{2+}$ label sequentially by specific recognition. The second procedure is the direct binding of amino-functionalized bead and the $[Ru(bpy)_3]^{2+}$ label through an amide covalent bond. The $[Ru(bpy)_3]^{2+}$-modified beads were deposited on a glassy carbon electrode where a constant voltage of 1.4 V was

applied. We selected this anodic potential because it generates strong and stable ECL intensity. The microscope setup records ECL images of the bead from the top-view and side-view configurations for dynamic analysis (Figure 1b). Since the beads modified by both labeling procedures showed similar photoluminescence (PL) and ECL behaviors, we kept the amide-modified beads in subsequent experiments to simplify the functionalization steps.
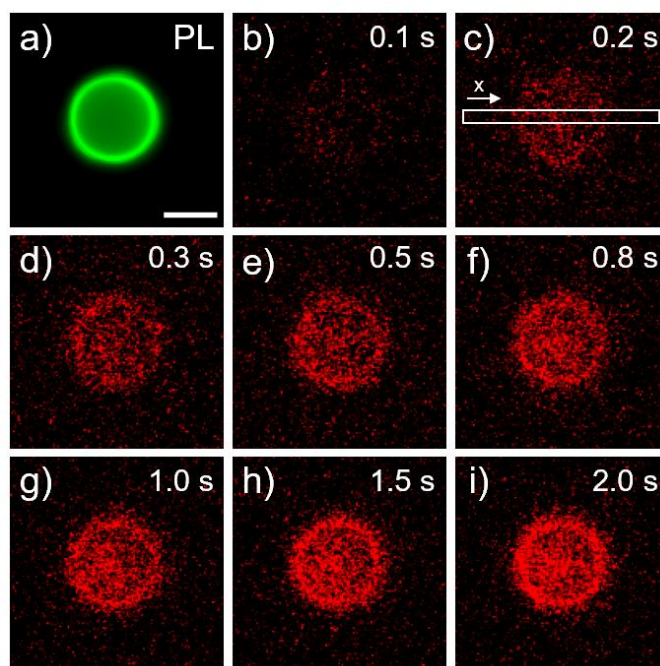

Figure 2. Dynamic recording of ECL mean intensity from a single $[Ru(bpy)_3]^{2+}$-decorated bead in the top-view configuration. (**a**) PL and (**b-i**) ECL images of a single labeled bead at different time points during the ECL process. Exposure time of each frame was 100 ms. The rectangle presents the region of interest where the ECL intensity profiles were extracted for Figure 3c. ECL was generated by imposing a constant potential of 1.4 V at a GC electrode in a PBS solution containing 100 mM TPA (pH 7.4). Scale bar: 10 µm.

The PL image in the top-view configuration indicates the location of the labeled bead on the electrode. The distribution of PL intensity shows the uniform $[Ru(bpy)_3]^{2+}$ decoration on the bead surface (Figure 2a). The high PL intensity at the bead edge is caused by the reflection of the optical signal inside the PS bead with high refractive index. To capture the full process of ECL behavior, a continuous recording of ECL images was started a few seconds before

electrical stimulation. Video S1 recorded the dynamic ECL behavior of a single bead. As illustrated by Figure 2b-2i, ECL intensity of each frame increased with time in the first 2 seconds. At t = 0.1 s, the ECL image does not reveal a clear spatial distribution due to the weak emission (Figure 2b). It means that, in 0.1 s, a part of $[Ru(bpy)_3]^{2+}$ labels have been converted into the excited state and emits light signals that are enough to be captured by the recording system. But at this time, the optical signals are still diffuse. The immobilized $[Ru(bpy)_3]^{2+}$ labels randomly react with the electrogenerated TPA radicals (TPA$^{\bullet}$ and TPA$^{\bullet+}$), leading to the formation of the excited state and *in fine* to dispersive light signals. Beyond t = 0.2 s, the flux of generated ECL photons is more important and the ECL images reveal the shape of a circled dot (Figure 2c-2i). The ECL pattern consists of a ring and a central spot. To quantify these varieties, a region of interest (ROI) along the *x*-axis on the bead was selected for extracting the ECL profile in each frame (Figure 2c). In fact, ECL intensity increased by 2-3 folds from 0.2 s to 2 s (Figure 3a). During this period, the ECL signal maintained the circled dot shape. In the top-view imaging, we can consider in a first order approximation that the central spot of ECL emission is formed by the overlay of the original light at the bottom part of the bead and the effects of the bead acting as a lens,[56] while the annular light band at the edge results from the complex optical paths in the bead. One can see that globally the same ECL pattern is maintained over time but with a progressive increase. The variation of the height of ECL emission layer (h_{ECL}) along the *z*-axis was calculated by extracting the diameter of the central spot over time (Figure S1). The value of h_{ECL} increased very rapidly in the first 0.2 s from 0.45 µm at t = 0.1 s to 1.6 at t = 0.2 s, reaching a quasi-plateau of 1.75 ± 0.34 µm for times longer than 0.2 s (Figure S1). This behavior implies that the ECL emission has complex dynamic changes over time (*vide infra*), which is hidden in conventional long-exposure static imaging.
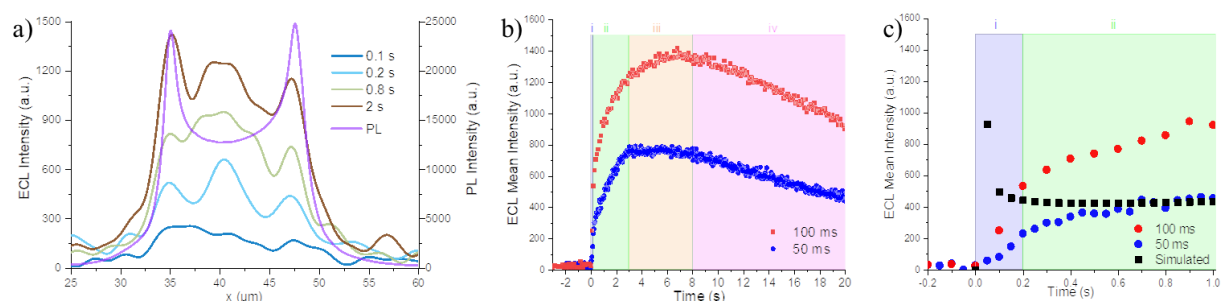
Figure 3. a) Dynamic of the ECL intensity profiles extracted along the *x*-axis. **b-c**) Comparison of the time-evolution of the ECL mean intensity from a single $[Ru(bpy)_3]^{2+}$-decorated bead in the top-view configuration with an exposure time of the EMCCD of 50 ms (blue dots) and 100 ms (red dots) with simulated data (black squares) considering the heterogeneous mechanism (*vide infra*). Same experimental conditions as in Figure 2.

We further quantified the kinetics of the ECL process by monitoring the time-evolution of ECL mean intensity (I_{ECL}) from a single $[Ru(bpy)_3]^{2+}$-decorated bead recorded with an exposure time of 100 ms (Figure 3b-c). The value of instantaneous I_{ECL} exhibited qualitatively four main phases: (i) a rapid ascent in the first 0.2 s; (ii) a slower increase; (iii) a quasi-plateau and (iv) a slow decrease of the ECL emission. The first phase (i) is very short and last for ~0.2 s. It is clearly visible when zooming in the first second of the process (Figure 3c). We checked that the duration of this phase was not convoluted by the exposure time of the EMCCD. For that, we repeated the experiments with a shorter exposure time of 50 ms. The same pattern was obtained for both exposure times. As expected, the ECL mean intensity was twice lower with an exposure time of 50 ms in comparison to 100 ms (Figure 3b-c). After this first phase, from approximately 0.2 s to 3-4 s, the ECL emission continues to increase but with a lower slope. Then, it reaches a quasi-plateau for 1-2 s (phase iii). The last phase (iv) occurs after 8 s with a slow decrease (Figure 3b). This complex behavior is rather unexpected considering the heterogeneous ECL mechanism operating in this experimental configuration with the immobilized labels on non-conductive beads. Since ECL is triggered by an initial electrochemical step, we recorded the chronoamperometric current (Figure S2**Please check**) during the imposition of the anodic pulse (1.4 V) used to capture the sequence of ECL images (Figure 2b-i). The current decreases monotonously over 20 s. The monotonic decrease of the current does not allow to interpret the observed evolution of the ECL signal.

To analyze further the ECL behavior, we considered that the ECL mechanism for emission of bead-immobilized $[Ru(bpy)_3]^{2+}$ labels follows the simplest heterogeneous pathway (also called the 'revisited' route) shown in Scheme 1:

(1) $TPA + H^+ \rightleftharpoons TPAH$

(2) $TPA - e^- \rightarrow TPA^{\bullet+}$

(3) $TPA^{\bullet+} \rightarrow TPA^{\bullet} + H^+$
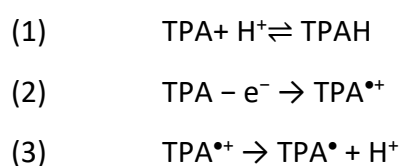
(4) $TPA^{\bullet} - e^{-} \rightarrow$ other products

(5) $[Ru(bpy)_3]^{2+} + TPA^{\bullet} \rightarrow [Ru(bpy)_3]^{+}$ + other products

(6) $[Ru(bpy)_3]^{+} + TPA^{\bullet+} \rightarrow [Ru(bpy)_3]^{2+*} + TPA$

(7) $[Ru(bpy)_3]^{2+*} \rightarrow [Ru(bpy)_3]^{2+} + h\nu$

Scheme 1. Heterogeneous $[Ru(bpy)_3]^{2+}$ and TPA co-reactant ECL mechanism.

In this heterogeneous pathway, $[Ru(bpy)_3]^{2+}$ is immobilized on the insulating PS bead (12 µm diameter) and a negligible fraction of the labels is within direct electron tunneling distance (~1-2 nm). In other words, an infinitesimal fraction of $[Ru(bpy)_3]^{2+}$ label can be directly oxidized at the electrode surface. Therefore, we can consider that the co-reactant is the only species directly oxidized at the electrode surface when imposing 1.4 V. This oxidation produces the cation $TPA^{\bullet+}$ radical (reaction 1) that later deprotonates rapidly (reaction 2) and forms the neutral $TPA^{\bullet}$ radical, which is a highly reducing species. The $TPA^{\bullet}$ radicals reduce the immobilized $[Ru(bpy)_3]^{2+}$ label to the $[Ru(bpy)_3]^{+}$ state (reaction 3). Finally, $[Ru(bpy)_3]^{+}$ reacts with the cation $TPA^{\bullet+}$ radical in the solution phase producing the surface-immobilized excited $[Ru(bpy)_3]^{2+*}$ state (reaction 4) of the label that generates ECL emission (reaction 5). The TPA co-reactant is the only diffusing species in this route and its electrogenerated radicals react with the immobilized labels. In brief, the reactivity of the cation $TPA^{\bullet+}$ radical governs mainly the heterogeneous ECL pathway. Its deprotonation is a fast process with an estimated rate constant of 2920 s^{-1} corresponding to a half-life time of ~0.24 ms. This short half-life time cannot explain the duration of the initial phases (i or/and ii) of the ECL process. In addition, we can estimate the time necessary for the electrogenerated species (i.e. TPA radicals) to diffuse from the electrode surface to the top of the bead, without, in a first order approximation, considering their intrinsic reactivity. We can reasonably assume that all the TPA species have a similar diffusion coefficient, i.e. $D = 5 \times 10^{-6}$ cm² s^{-1} in water.[57] The diameter of the beads (12 µm) translates into a diffusion time of ~90 ms necessary for the TPA radicals to reach the top of the bead, again without taking into account their chemical reactivity. It is approximately two times shorter than the duration of phase i (Figure 3c). This time is even shorter (Figure 3c) if we consider the results of the simulations of the ECL mechanism operating at the bead level (*vide infra*).

To obtain accurate spatial information, we recorded the dynamic ECL behavior of $[Ru(bpy)_3]^{2+}$-labeled bead under an orthogonal side-view configuration (Figure 1b). Figure 4a shows a set of images. In the PL image (left, green), the upper part is the real physical location of the bead that can help confirm the boundary, while the lower part is the reflection of the bead on the glassy carbon electrode surface. The corresponding ECL images (red) of the bead exhibit that the real light signal comes from ~3 μm from the electrode surface, and the signal at the top is the focused light due to the lens effect of the PS material. Since the signal captured in the side view is limited, the ECL intensity is weaker than that from the top view. So, the single-frame exposure time is increased to 300 ms, for the sake of image quality. The ECL profile of the bead along the *z*-axis was extracted (Figure S3**PLEASE CHECK**). By positioning the peak value of the profile, the height of maximum ECL emission ($h_{Max-ECL}$) was measured (Figure S4 **PLEASE CHECK**). One can observe that at the initial stage of the reaction, the maximum intensity and $h_{Max-ECL}$ vary with time (Figure 4b). It indicates the excitation rate of $[Ru(bpy)_3]^{2+}$ changes over time, which may be related to the variation of the deprotonation rate of the TPA cation radical or to the chemical reactivity of the electrode surface.
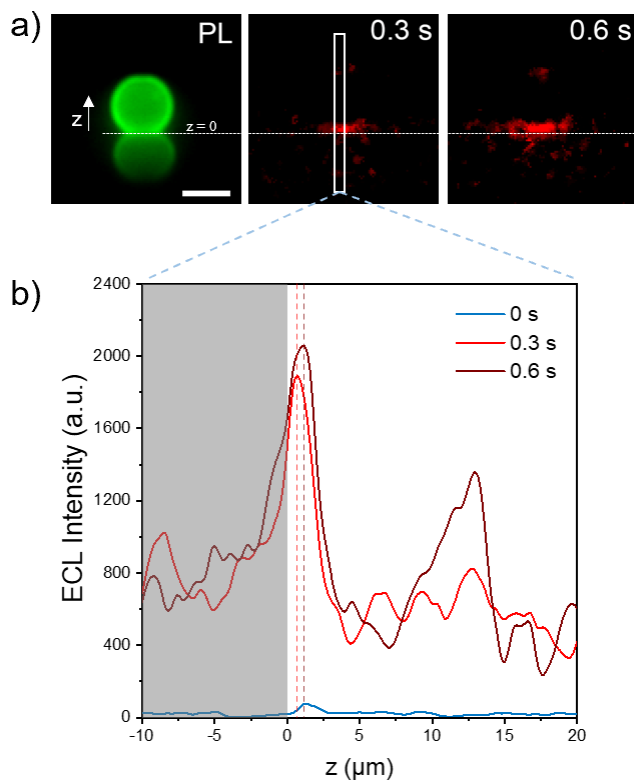
Figure 4. a) PL (green color) and ECL (red color) images of the same single $[Ru(bpy)_3]^{2+}$-labeled bead in the side-view configuration during the ECL process. The rectangle presents the ROI where (**b**) ECL profiles were extracted. The dotted lines indicate the peaks of the ECL profiles. ECL was generated by imposing a constant potential of 1.4 V with a GC electrode in a PBS solution containing 100 mM TPA (pH 7.4). Exposure time for each ECL image: 300 ms. Scale bar: 10 µm.

In an attempt to explain the kinetics of the heterogeneous ECL process we used numerical digital simulation to model the kinetics of the ECL signal generated at the level of the functionalized beads (see *table S1-S5 and figure S5-S10 and* supporting information for details). Finite element simulation is a powerful tool to analyze the concentration profile and the ECL distribution.[58, 59] According to the reaction mechanism (Scheme 1), the generation of the luminophore excited state requires the presence of both the strong reducing radical TPrA$^{\bullet}$ and the strong oxidizing radical cation TPrA$^{\bullet+}$ generated from the electrode surface. These concentration profiles reach a steady state, and with this the ECL intensity, within the first second of the electrochemical stimulation (Video S2, S3). Figure 5a and 5b present the

simulated ECL mapping at t = 1 s from top view and side view, respectively. It could be seen that the emission layer is annularly distributed at the bottom of the bead with intensity gradients. Such gradients are not obvious in the experimental ECL images, due to the overlay of lights. In the simulation, h_{ECL} and $h_{Max-ECL}$ reached a plateau at t = 0.2 s and t = 0.01 s, respectively, while in the experiments, h_{ECL} and $h_{Max-ECL}$ peaked around t = 0.8 s and t = 0.6 s (Figure 5c). In general, the value of h_{ECL} reflects the kinetic rate of TPA$^{•+}$ deprotonation, and the position of $h_{Max-ECL}$ depends on the equilibrium concentration of TPA$^{•+}$ and TPA$^{•}$.[56, 60] In the simulation, both h_{ECL} and $h_{Max-ECL}$ remain constant soon after the initial increase.
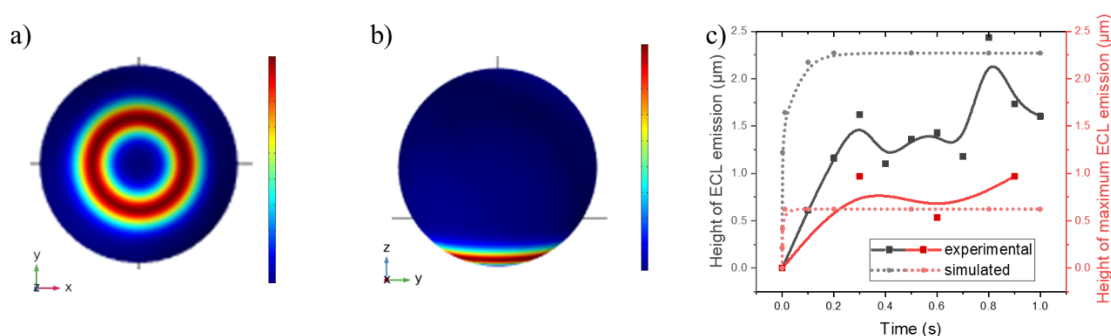

Figure 5. Simulated mapping of the generated [Ru(bpy)$_3$]$^{2+}$* excited state (*i.e.,* ECL intensity) at the surface of a 12-µm bead in top (**a**) and side-view (**b**) configurations at t = 1 s after the anodic potential pulse. **c**) Evolution of the height of ECL emission (h_{ECL}) over time of the simulation (black circles) and the experimental data (black squares) as well as the height of maximum ECL emission ($h_{Max-ECL}$) in the simulation (red circles) and the experiment (red squares) of a 12-µm bead.

Under the simulated conditions, the extremely large oxidation rate of TPA at the very beginning results in a burst of ECL intensity at t = 0.05 s, and then quickly falls back and stabilizes at a certain value (Figure 3c). Nevertheless, in the actual experiments, ECL signal continued to climb several seconds when potential was applied. The observed difference between the experimental data and the simulation may be explained by the evolution of the GC surface towards the oxidation of TPA, as reported previously during successive anodic pulses.[55] Another hypothesis is related to the experimental configuration used to record the

ECL images. Indeed, for the simulation, bulk conditions (i.e., infinite volume of solution above the bead) are used whereas, for the ECL imaging, it corresponds more to a thin layer cell because there is a glass coverslip between the microscope objective and the electrode surface with the beads. Whatever, these results demonstrate the unique advantages of dynamic ECL imaging in revealing kinetics of the ECL process. In the future, this method should be able to provide a variety of dynamic messages for more ECL systems with different conditions and help to understand the ECL mechanism and reveal transient information.

Conclusion

In this work, we recorded the time evolution of bead-based ECL process. Dynamic information such as the behavior of instantaneous ECL intensity, the height of ECL layer and the location of maximum ECL emission over time is displayed, which was not achieved by previous static imaging. Based on the parameters obtained above, the kinetic of the co-reactant and luminophore during the ECL reactivity was studied. In comparison to simulation, the factors affecting ECL behavior in experimental conditions were found, which provide a reference for the optimization of existing bead-based ECL immunoassays. Differences between the experimental results and the simulation were observed at short times and, even if further surface studies are required, they could be related to the evolution of the GC surface towards the oxidation of TPA. Finally, the dynamic ECL imaging approach is expected to help with more kinetics studies of ECL systems and new reaction mechanisms.

Acknowledgements

Supporting Information

Simulations. ECL data. Chronoamperometric current.

References

(1) Liu, Z.; Qi, W.; Xu, G. *Chem. Soc. Rev.* **2015**, *44*, 3117-3142.

(2) Zhang, J.; Arbault, S.; Sojic, N.; Jiang, D. *Annu. Rev. Anal. Chem.* **2019**, *12*, 275-295.

(3) Zanut, A.; Fiorani, A.; Rebeccani, S.; Kesarkar, S.; Valenti, G. *Anal. Bioanal. Chem.* **2019**, *411*, 4375-4382.

(4) Dong, J. L., Y.; Xu, Y.; Chen, F.; Yang, J.; Chen, Y.; Feng, J. *Nature* **2021**, *596*, 244-249.

(5) Ma, C.; Cao, Y.; Gou, X.; Zhu, J.-J. *Anal. Chem.* **2020**, *92*, 431-454.

(6) Fang, Y.; Zhou, Z.; Hou, Y.; Wang, C.; Cao, X.; Liu, S.; Shen, Y.; Zhang, Y. *Anal. Chem.* **2023**, *95*, 6620-6628.

(7) Du, F.; Chen, Y.; Meng, C.; Lou, B.; Zhang, W.; Xu, G. *Curr. Opin. Electrochem.* **2021**, *28*, 100725.

(8) Zanut, A.; Fiorani, A.; Canola, S.; Saito, T.; Ziebart, N.; Rapino, S.; Rebeccani, S.; Barbon, A.; Irie, T.; Josel, H.-P.; et al. *Nat. Commun.* **2020**, *11*, 2668.

(9) Sakanoue, K.; Fiorani, A.; Santo, C. I.; Irkham; Valenti, G.; Paolucci, F.; Einaga, Y. *ACS Sens.* **2022**, *7*, 1145-1155.

(10) Qi, H.; Zhang, C. *Anal. Chem.* **2020**, *92*, 524-534.

(11) Amatore, C.; Pebay, C.; Servant, L.; Sojic, N.; Szunerits, S.; Thouin, L. *ChemPhysChem* **2006**, *7*, 1322–1327.

(12) Chen, M.-M.; Xu, C.-H.; Zhao, W.; Chen, H.-Y.; Xu, J.-J. *J. Am. Chem. Soc.* **2021**, *143*, 18511-18518.

(13) Kanoufi, F.; Sojic, N. *Nature* **2021**, *596*, 194-195.

(14) Rebeccani, S.; Zanut, A.; Santo, C. I.; Valenti, G.; Paolucci, F. *Anal. Chem.* **2021**, *94*, 336-348.

(15) Liu, Y.; Zhang, H.; Li, B.; Liu, J.; Jiang, D.; Liu, B.; Sojic, N. *J. Am. Chem. Soc.* **2021**, *143*, 17910-17914.

(16) Li, B.; Huang, X.; Lu, Y.; Fan, Z.; Li, B.; Jiang, D.; Sojic, N.; Liu, B. *Adv. Sci. (Weinh)* **2022**, *9*, e2204715.

(17) Fiorani, A.; Han, D.; Jiang, D.; Fang, D.; Paolucci, F.; Sojic, N.; Valenti, G. *Chem. Sci.* **2020**, *11*, 10496-10500.

(18) Xu, L.; Li, Y.; Wu, S.; Liu, X.; Su, B. *Angew. Chem. Int. Ed.* **2012**, *51*, 8068-8072.

(19) Zhu, M.-J.; Pan, J.-B.; Wu, Z.-Q.; Gao, X.-Y.; Zhao, W.; Xia, X.-H.; Xu, J.-J.; Chen, H.-Y. *Angew. Chem. Int. Ed.* **2018**, *57*, 4010-4014.

(20) Zhu, H.; Jiang, D.; Zhu, J.-J. *Chem. Sci.* **2021**, *12*, 4794-4799.

(21) Han, D.; Goudeau, B.; Lapeyre, V.; Ravaine, V.; Jiang, D.; Fang, D.; Sojic, N. *Biosens. Bioelectron.* **2022**, *216*, 114640.

(22) Ma, C.; Wu, S.; Zhou, Y.; Wei, H.-F.; Zhang, J.; Chen, Z.; Zhu, J.-J.; Lin, Y.; Zhu, W. *Angew. Chem. Int. Ed.* **2021**, *60*, 4907-4914.

(23) Chovin, A.; Garrigue, P.; Sojic, N. *Electrochim. Acta* **2004**, *49*, 3751–3757.

(24) Sentic, M.; Virgilio, F.; Zanut, A.; Manojlovic, D.; Arbault, S.; Tormen, M.; Sojic, N.; Ugo, P. *Anal. Bioanal. Chem.* **2016**, *408*, 7085-7094.

(25) Li, H.; Bouffier, L.; Arbault, S.; Kuhn, A.; Hogan, C. F.; Sojic, N. *Electrochem. commun.* **2017**, *77*, 10-13.

(26) Chovin, A.; Garrigue, P.; Sojic, N. *Electrochim. Acta* **2004**, *49*, 3751-3757.

(27) Guo, W.; Ding, H.; Zhou, P.; Wang, Y.; Su, B. *Angew. Chem. Int. Ed.* **2020**, *59*, 6745-6749.

(28) Zhao, W.; Chen, H.-Y.; Xu, J.-J. *Chem. Sci.* **2021**, *12*, 5720-5736.

(29) Guo, W.; Zhou, P.; Sun, L.; Ding, H.; Su, B. *Angew. Chem. Int. Ed.* **2021**, *60*, 2089-2093.

(30) Ding, H.; Guo, W.; Su, B. *Angew. Chem. Int. Ed.* **2020**, *59*, 449-456.

(31) Ding, H.; Zhou, P.; Fu, W.; Ding, L.; Guo, W.; Su, B. *Angew. Chem. Int. Ed.* **2021**, *60*, 11769-11773.

(32) Ma, Y.; Colin, C.; Descamps, J.; Arbault, S.; Sojic, N. *Angew. Chem. Int. Ed.* **2021**, *60*, 18742-18749.

(33) Glasscott, M. W.; Voci, S.; Kauffmann, P. J.; Chapoval, A. I.; Dick, J. E. *Langmuir* **2021**, *37*, 2907-2912.

(34) Glasscott, M. W.; Dick, J. E. *J. Phys. Chem. Lett.* **2020**, *11*, 4803-4808.

(35) Gou, X.; Xing, Z.; Ma, C.; Zhu, J.-J. *Chem. Biomed. Imaging* **2023**.

(36) Guo, M.; Du, D.; Wang, J.; Ma, Y.; Yang, D.; Haghighatbin, M. A.; Shu, J.; Nie, W.; Zhang, R.; Bian, Z.; et al. *Chem. Biomed. Imaging* **2023**, *1*, 179-185.

(37) Dong, J.; Xu, Y.; Zhang, Z.; Feng, J. *Angew. Chem. Int. Ed.* **2022**, *61*, e202200187.

(38) Valenti, G.; Scarabino, S.; Goudeau, B.; Lesch, A.; Jović, M.; Villani, E.; Sentic, M.; Rapino, S.; Arbault, S.; Paolucci, F.; et al. *J. Am. Chem. Soc.* **2017**, *139*, 16830-16837.

(39) Voci, S.; Goudeau, B.; Valenti, G.; Lesch, A.; Jović, M.; Rapino, S.; Paolucci, F.; Arbault, S.; Sojic, N. *J. Am. Chem. Soc.* **2018**, *140*, 14753-14760.

(40) Ma, C.; Wei, H.-F.; Wang, M.-X.; Wu, S.; Chang, Y.-C.; Zhang, J.; Jiang, L.-P.; Zhu, W.; Chen, Z.; Lin, Y. *Nano Lett.* **2020**, *20*, 5008-5016.

(41) Ma, C.; Wu, W.; Li, L.; Wu, S.; Zhang, J.; Chen, Z.; Zhu, J.-J. *Chem. Sci.* **2018**, *9*, 6167-6175.

(42) Wu, K.; Chen, R.; Zhou, Z.; Chen, X.; Lv, Y.; Ma, J.; Shen, Y.; Liu, S.; Zhang, Y. *Angew. Chem. Int. Ed.* **2023**, *62*, e202217078.

(43) Kerr, E.; Hayne, D. J.; Soulsby, L. C.; Bawden, J. C.; Blom, S. J.; Doeven, E. H.; Henderson, L. C.; Hogan, C. F.; Francis, P. S. *Chem. Sci.* **2022**, *13*, 469-477.

(44) Haghighatbin, M. A.; Laird, S. E.; Hogan, C. F. *Curr. Opin. Electrochem.* **2018**, *7*, 216-223.

(45) Zanut, A.; Palomba, F.; Rossi Scota, M.; Rebeccani, S.; Marcaccio, M.; Genovese, D.; Rampazzo, E.; Valenti, G.; Paolucci, F.; Prodi, L. *Angew. Chem. Int. Ed.* **2020**, *59*, 21858 – 21863.

(46) Rebeccani, S.; Wetzl, C.; Zamolo, V. A.; Criado, A.; Valenti, G.; Paolucci, F.; Prato, M. *Chem. Comm.* **2021**, *57*, 9672-9675.

(47) Deiss, F.; LaFratta, C. N.; Symer, M.; Blicharz, T. M.; Sojic, N.; Walt, D. R. *J. Am. Chem. Soc.* **2009**, *131*, 6088-6089.

(48) Miao, W.; Choi, J.-P.; Bard, A. J. *J. Am. Chem. Soc.* **2002**, *124*, 14478-14485.

(49) Sentic, M.; Milutinovic, M.; Kanoufi, F.; Manojlovic, D.; Arbault, S.; Sojic, N. *Chem. Sci.* **2014**, *5*, 2568-2572.

(50) Sojic, N. Analytical Electrogenerated Chemiluminescence: From Fundamentals to Bioassays; Royal Society of Chemistry, **2019**.

(51) Miao, W.; Choi, J.-P.; Bard, A. J. *J. Am. Chem. Soc.* **2002**, *124*, 14478-14485.

(52) Wang, Y.; Ding, J.; Zhou, P.; Liu, J.; Qiao, Z.; Yu, K.; Jiang, J.; Su, B. *Angew. Chem. Int. Ed.* **2023**, *62*, e202216525.

(53) Guo, W.; Zhou, P.; Sun, L.; Ding, H.; Su, B. *Angew. Chem. Int. Ed.* **2021**, *60*, 2089-2093.

(54) Dutta, P.; Han, D.; Goudeau, B.; Jiang, D.; Fang, D.; Sojic, N. *Biosens. Bioelectron.* **2020**, *165*, 112372.

(55) Han, D.; Goudeau, B.; Jiang, D.; Fang, D.; Sojic, N. *Anal. Chem.* **2021**, *93*, 1652-1657.

(56) Sentic, M.; Milutinovic, M.; Kanoufi, F.; Manojlovic, D.; Arbault, S.; Sojic, N. *Chem. Sci.* **2014**, *5*, 2568-2572.

(57) Miao, W.; Choi, J. P.; Bard, A. J. *J. Am. Chem. Soc.* **2002**, *124*, 14478-14485.

(58) Daviddi, E.; Oleinick, A.; Svir, I.; Valenti, G.; Paolucci, F.; Amatore, C. *ChemElectroChem* **2017**, *4*, 1719-1730.

(59) Imai, K.; Valenti, G.; Villani, E.; Rapino, S.; Rampazzo, E.; Marcaccio, M.; Prodi, L.; Paolucci, F. *J. Phys. Chem. C* **2015**, *119*, 26111-26118.

(60) Fiorani, A.; Han, D.; Jiang, D.; Fang, D.; Paolucci, F.; Sojic, N.; Valenti, G. *Chem. Sci.* **2020**, *11,* 10496.

Table of Contents (TOC)